The Astrophysical Journal, 944:62 (14pp), 2023 February 10 https://doi.org/10.3847/1538-4357/acac32

Nonthermal X-Rays from Pulsation-driven Shocks in Cepheids

Federico Fraschetti[1,2], Konstantina Anastasopoulou[2], Jeremy J. Drake[2], and Nancy Remage Evans[1]
[1] Center for Astrophysics | Harvard & Smithsonian, 60 Garden Street, Cambridge MA, 02138, USA; federico.fraschetti@cfa.harvard.edu
[2] Department of Planetary Sciences—Lunar and Planetary Lab, Tucson, AZ, 85721, USA
Received 2022 November 5; revised 2022 December 13; accepted 2022 December 13; published 2023 February 13

Abstract

Rapid X-ray phase-dependent flux enhancement in the archetype classical Cepheid star δ Cep was observed by XMM-Newton and Chandra. We jointly analyze thermal and nonthermal components of the time-resolved X-ray spectra prior to, during, and after the enhancement. A comparison of the timescales of shock particle acceleration and energy losses is consistent with the scenario of a pulsation-driven shock wave traveling into the stellar corona and accelerating electrons to ∼GeV energies, and with Inverse Compton (IC) emission from the UV stellar background leading to the observed X-ray enhancement. The index of the nonthermal IC photon spectrum, assumed to be a simple power law in the [1–8] keV energy range, radially integrated within the shell [3–10] stellar radii, is consistent with an enhanced X-ray spectrum powered by shock-accelerated electrons. An unlikely ∼100-fold amplification via turbulent dynamo of the magnetic field at the shock propagating through density inhomogeneities in the stellar corona is required for the synchrotron emission to dominate over the IC; the lack of time correlation between radio synchrotron and stellar pulsation contributes to make synchrotron as an unlikely emission mechanism for the flux enhancement. Although current observations cannot rule out a high-flux two-temperature thermal spectrum with a negligible nonthermal component, this event might confirm for the first time the association of Cepheids pulsation with shock-accelerated GeV electrons.

Unified Astronomy Thesaurus concepts: Cepheid variable stars (218); Shocks (2086); X-ray transient sources (1852)

1. Introduction

Rapid time variability in X-ray flux has proven a valuable approach to constrain the physical properties of a variety of astrophysical sources, from jets in Active Galactic Nuclei (e.g., Markowitz et al. 2022), black hole accretion discs (e.g., Wilkinson & Uttley 2009), tidal disruption events (Hampel et al. 2022), accreting neutron stars emitting Type-I X-ray bursts from the surface (Degenaar et al. 2018), or protostellar disk chemically affected by stellar flares (Cleeves et al. 2017). Time variability has also enabled X-rays observations to probe the particle acceleration in shock-driven plasmas, as opposed to, e.g., magnetic reconnection: variability on a year timescale in the X-ray filaments of the supernova remnant Cassiopeia A was associated (Uchiyama & Aharonian 2008) with fast synchrotron cooling in strong magnetic field; variability on a year timescale at inward shocks of Cas A (Sato et al. 2018) allowed to constrain overdensities in shocked ejecta, small-scale dynamo processes, and particle acceleration therein (Fraschetti et al. 2018); a ∼3 day drop in the plasma temperature behind the shock possibly generated by the outburst of the Nova V745 Sco was jointly observed by Swift, Chandra, and NuStar (Drake et al. 2016) and attributed to the leak of a substantial energy fraction in the form of cosmic rays (protons and heavier ions); laboratory astrophysics experiments have identified via X-ray diagnostics the dynamo mechanism rapidly amplifying magnetic fields at shock waves (e.g., Meinecke et al. 2014).

The luminous pulsating Cepheid supergiants have shown in recent years a surprising X-ray variability correlated with pulsation phase. Combined XMM-Newton and Chandra observations have shown an unexpected fourfold enhancement of the (0.3–2.5) keV X-ray flux from the archetype Cepheid δ Cep (Engle et al. 2017) over ∼0.2 in pulsation phase (pulsation period ∼5.37 days; Engle et al. 2017); the enhancement is observed at the phase of the maximum radius. Chandra also detected a rapid increase of X-ray flux in β Doradus at the phase of maximal radius (Evans et al. 2018). However, lack of X-ray enhancement at the same phase was reported from XMM-Newton for the Cepheid η Aql (Evans et al. 2021).

A rapid enhancement in X-ray flux in Cepheids could be due to pulsation-driven compression of the magnetic field leading to reconnection, as in solar flares, or to the propagation of pulsation-driven shocks, either of which could plausibly heat gas to UV and X-ray emitting temperatures (10^4–10^6 K). The latter scenario was investigated in detail by Moschou et al. (2020), who showed that observed phase-dependent X-ray enhancements could be the result of pulsation-driven shock heating of ambient hot plasma. Here, we aim to build on that work by examining whether or not such shocks could also produce efficiently a population of accelerated particles—and potentially, nonthermal X-ray emission.

In considering possible particle acceleration in Cepheid atmospheric shocks, it is also useful to recall the circumstellar environments and radiatively driven winds of early-type stars that are likely to be permeated by traveling shocks, owing to the "line deshadowing instability" (Lucy & Solomon 1970; Owocki 2015). Lucy & White (1980) and Lucy (1982a, 1982b) built a phenomenological model for the soft X-ray emission from gas heated by radiation-driven shock waves traveling into the gas at the base of the wind: the gas re-emits in the soft X-ray band via collisional excitation of ionized heavy ions. A key assumption is that the radiative cooling time is much

shorter than the time between two subsequent shocks, which can therefore be considered isothermal. This mechanism based on radiation-driven shocks was revised to interpret the hard X-ray (Chen & White 1991a) and γ-ray emission (Chen & White 1991b) from OB supergiants as Inverse Compton (IC) emission from the UV field photons upscattered by shock-accelerated electrons.

In the Lucy & White (1980) mechanism, the instabilities produce compressive waves that steepen into shocks propagating outward. In stars as cool as Cepheids, winds are not thought to be driven by resonance lines that might drive shocks via the line deshadowing instability; however, evidence of traveling shocks driven by pulsation within a number of Cepheids has been collected in recent years. Cuntz & Luttermoser (1990) modelled the formation of the chromospheric He I λ 10830 line in late-type cool giant stars via shock heating. Bohm-Vitense & Love (1994) found that steep increases in emission-line fluxes $\sim$0.1 phase before the peak of light for the Cepheid l Carinae suggest emission from a chromospheric shock wave moving at speed greater than 100 km s^{-1}, i.e., on the order of the escape velocity. Sasselov & Lester (1994) applied coupled hydrodynamics and non-LTE radiative transfer modeling of chromospheric emission lines and concluded that Cepheids have chromospheres heated by acoustic or magnetic wave dissipation in addition to transient heating driven by the pulsation dynamics. Mathias et al. (2006) found evidence of two consecutive shocks per pulsation period at X Sagittarii from analysis of spectral lines obtained using the HARPS spectrograph. Nardetto et al. (2006) found broadening of metal lines in RS Pup and suggested this was evidence of compressions or shock waves traveling through the stellar atmosphere.

In this paper, we present a new analysis of the thermal and possible nonthermal components of the X-ray spectrum of δ Cep during the flux enhancements observed by Chandra and XMM-Newton (Engle et al. 2017), in order to place constraints on nonthermal emission and the underlying energetic electron population. We also compare acceleration and energy-loss timescales for electrons accelerated at the pulsation-driven shocks to identify plausible mechanisms of nonthermal emission. We find that the timescale of IC scattering of the UV photons from the stellar radiation field off the shock-accelerated electrons could potentially give rise to rapid nonthermal flux increases.

The structure of this paper is as follows: in Section 2, the high- and low-state photon spectra are fitted with a thermal/nonthermal model and with a two-temperature model. In Section 3, the timescales for radiative cooling and electron shock acceleration are compared with a variety of energy losses processes. In Section 4, the results are discussed, followed by our conclusions in Section 5.

2. X-Ray observations

Engle et al. (2014) analyzed the X-ray observations of δ Cep using a two-temperature thermal spectral model to calculate the flux. In order to obtain observational constraints on the possible presence of nonthermal X-ray emission, we have performed a new analysis of the XMM-Newton data, combining a thermal and a power-law spectral model. We reanalyze the five observations of XMM-Newton, and fit separately the high-flux ($f_{0.3\text{–}2.5\ \mathrm{keV}} > 8\times10^{-15}$ erg s^{-1} cm^{-2}) and the low-flux ($f_{0.3\text{–}2.5\ \mathrm{keV}} < 8\times10^{-15}$ erg s^{-1} cm^{-2}) observations according to the flux measurements nomenclature of Engle et al. (2014, 2017) but without splitting the single observations (see Figure 1). Low- and high-flux observations are fitted separately to identify different physical mechanisms—thermal and nonthermal—that could be imprinted in the spectra. Our analysis shows that, for a one-temperature thermal spectral model, the X-ray flux above $\sim$1 keV is significantly in excess of the thermal flux and the spectrum of such a hard component can be fitted with a single power law in the range [1–8] keV. We show in Table 1 the XMM-Newton observation IDs and the exposure times corresponding to each of the three EPIC detectors after cleaning for background flares. We have used the ephemeris reported in Table 1 of Engle et al. (2014), namely $t(\mathrm{obs}) = 2455479.905 + 5.366208(14)\times E$ days, where t(obs) is the time of the observation, 2455479.905 days is the time of a known past maximum light, $t_p = 5.366208(14)$ days, and E is the epoch; the phase in Figure 1 is the decimal part of E.

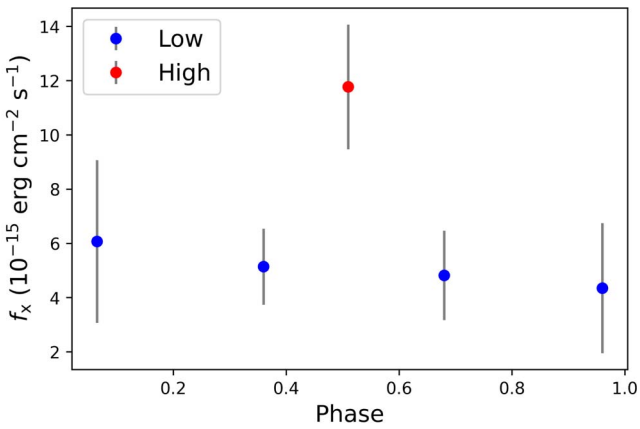

Figure 1. The X-ray flux vs. pulsation phase from the XMM-Newton observations of δ Cep used in this study, based on the fluxes and phases presented in Engle et al. (2017). Phase = 0 corresponds to maximum light. We present the average flux and phase values of observations that were split in Engle et al. (2017). "Low" and "High" 0.3–2.5 keV flux designations for the different observations are shown with red and blue dots, respectively.

2.1. Calibration and Spectral Extraction

We reduced and analyzed all EPIC archival observations for δ Cep using the XMM-Newton Science Analysis System (SAS) v17.0.0. Calibrated event files were produced using the SAS tasks *emchain* and *epchain* for the MOS and pn cameras respectively. Moreover, out-of-time event files were created for the pn camera using *epchain* and *withoutoftime* = *Y*, in order to subtract out-of-time events and correct for the charge transfer inefficiency. The tool *emtaglenoise* was used in order to flag noisy MOS CCDs at low energies (Kuntz & Snowden 2008).

We filtered background flares by creating good time interval (GTI) files using the SAS task *tabgtigen* with a cutoff of 2.5 counts s^{-1} for the MOS and 8.0 counts s^{-1} for the pn camera. We created a background lightcurve for each detector, which was visually inspected to ensure the proper removal of the background flares. This resulted in filtered event lists for the pn and MOS cameras.

We then extracted spectra and calibration files for all the observations of δ Cep. In order to extract the source and background spectra, we used the *evselect* SAS task, and limited the patterns to singles and doubles for both EPIC pn and MOS event files. For the extraction of the background spectra, we selected a region nearby the source, making sure we were not including any background sources. We then extracted the Auxiliary Response Files (ARF) and the Redistribution Matrix

Table 1
Summary of δ Cepheid XMM-Newton Listing Observation ID, Start and End Dates, and Clean Exposure Times in the MOS and pn Cameras.

Observation ID	Start Date	End Date	Exp pn (s)	Exp MOS1 (s)	Exp MOS2 (s)
		High-flux			
0603741001	2010-1-22 18:05:45	2010-1-23 14:17:43	69820	72146	72146
		Low-flux			
0552410401	2008-6-05 14:26:02	2008-6-05 21:53:07	24685	26112	26107
0603740901	2010-1-20 18:04:11	2010-1-21 12:37:47	49019	56208	56483
0723540301	2013-6-28 06:11:55	2013-6-29 14:54:45	103583	106436	106492
0723540401	2013-7-02 05:37:02	2013-7-03 08:00:22	92020	93613	93620

Table 2
Best-fit Parameters from Spectral Fitting of the High-flux and Low-flux Observations.

Model	$N_{\rm H}$ 10^{22} atoms cm^{-2}	kT_1 keV	normkT_1 $\times10^{-4}$	kT_2 keV	normkT_2 $\times10^{-5}$	norm$_\Gamma$ $\times10^{4}$	χ^2 (dof)	χ^2_ν
			High-flux					
tbabs×(apec+apec)	$0.79^{+0.47}_{-0.24}$	0.11 ± 0.04	>35.0	$0.57^{+0.74}_{-0.27}$	$2.4^{+13.6}_{-1.2}$	⋯	15.0 (19)	0.79
tbabs×(bknpower+apec) ($\Gamma=2.0$)	0.85 ± 0.09	0.17 ± 0.03	$8.7^{+17.6}_{-5.4}$	⋯	⋯	1.2 ± 0.6	25.5 (20)	1.27
tbabs×(bknpower+apec) ($\Gamma=1.8$)	0.86 ± 0.09	0.17 ± 0.03	$8.9^{+16.4}_{-5.4}$	⋯	⋯	0.9 ± 0.5	25.8 (20)	1.29
tbabs×(bknpower+apec) ($\Gamma=1.6$)	0.87 ± 0.09	0.17 ± 0.03	$8.9^{+15.2}_{-5.5}$	⋯	⋯	0.6 ± 0.4	26.4 (20)	1.32
			Low-flux					
tbabs×(apec+apec) (incl. 0552410401)	$0.61^{+0.53}_{-0.35}$	$0.15^{+0.10}_{-0.06}$	>2.3	$0.62^{+0.85}_{-0.23}$	$0.6^{+3.1}_{-0.2}$	⋯	33.58 (30)	1.12
tbabs×(apec+apec) (excl. 0552410401)	$0.63^{+0.67}_{-0.34}$	$0.14^{+0.09}_{-0.06}$	>2.4	$0.59^{+0.75}_{-0.22}$	$0.7^{+2.3}_{-0.4}$	⋯	28.0 (26)	1.07

Note. The normalization of the APEC component is in units of $\frac{10^{-14}}{4\pi D^2}\int n_e n_{\rm H} dV$, where n_e and $n_{\rm H}$ are the electron and hydrogen densities integrated over the volume V of the emitting region and D is the distance to the source in cm. The normalization of the power law is in units of photons keV^{-1} cm^{-2} s^{-1} at 1 keV.

Files (RMF) for the source spectra using the SAS task *arfgen* and *rmfgen*, respectively.

For the fitting of the spectra, we have used the XSPEC v12.11.1 software (Arnaud 1996). In order to allow for chi-square fitting, we grouped the spectra in bins of 25 total counts. For the high-flux spectra (see Table 1), we fitted simultaneously the spectra from all EPIC detectors with all model parameters tied together. We also introduced a multiplicative constant, frozen to unity for pn and free for the MOS detectors, that was applied to each spectrum in order to account for residual calibration offsets between the different detectors. For the low-flux spectra, we used only the pn detector because the MOS detectors had very few counts. A multiplicative constant was introduced as well, but this time to account for differences in the long-term variability, or long-term residual variations in the calibration. The line-of-sight Galactic absorption was in each case let free to vary.

In Table 2, we report our spectral fitting results for the best-fit models of the high- and low-flux spectra, respectively. The multiplicative parameters show in all cases a difference of about 10%–15% between pn and MOS detectors. For the low-flux pn observations, the multiplicative parameters do not differ in any case more than 4%.

2.2. High-flux Spectrum

A two-component thermal model was used by Engle et al. (2014) to fit the X-ray spectrum of δ Cepheid. Indeed, in the case of the high-flux observation, a best-fit single thermal component with temperature of $kT=0.18$ keV does not provide a satisfactory fit to the spectrum ($\chi^2_\nu>1.6$) with residuals below 0.6 keV and above 1.5 keV. If a second empirical thermal component is introduced (model in XSPEC: tbabs×(apec+apec)), the fit significantly improves, with $\chi^2_\nu=0.79$ and temperatures of $kT_1=0.12$ keV and $kT_2=0.60$ keV .

In order to explore the contribution of a possible nonthermal component at higher energies (>1.5 keV) we introduced a "broken power-law" model (model in XSPEC: tbabs×(bknpower+apec)) where the power-law photon index Γ above a certain energy break E_0 is positive (declining spectrum at large energy) and below E_0 it is frozen to a negative value in order to suppress the spectrum at soft energies. The energy break and the power-law photon index Γ for $E>E_0$ are frozen at $E_0=0.8$ keV and $\Gamma=2.0$ or 1.8 or 1.6, respectively. Such values follow from the timescale analysis in Sections 3 and 4 that supports a nonthermal emission originating from IC off the UV stellar radiation field. Small variations in the value of the E_0 (±0.3 keV) do not significantly alter the fitting results. The thermal plus power-law model gives an acceptable fit of $\chi^2_\nu=1.27$ or 1.29 or 1.32 for $\Gamma=2.0$ or 1.8 or 1.6 (see table 2). These fits include all EPIC detectors (pn, MOS1, and MOS2). The column density $N_{\rm H}$ best-fit value of the two-temperature fit is not statistically different from the one of the thermal+power-law fit. From the best-fit model, we find that the contribution of the nonthermal flux to the energy-integrated source flux in the 0.3–10 keV band is as large as ∼30% . We present the results of the best-fitting models in the first four rows of Table 2 (we also report the best-fit values for $\Gamma=1.8$ and $\Gamma=1.6$) and in Figure 2.

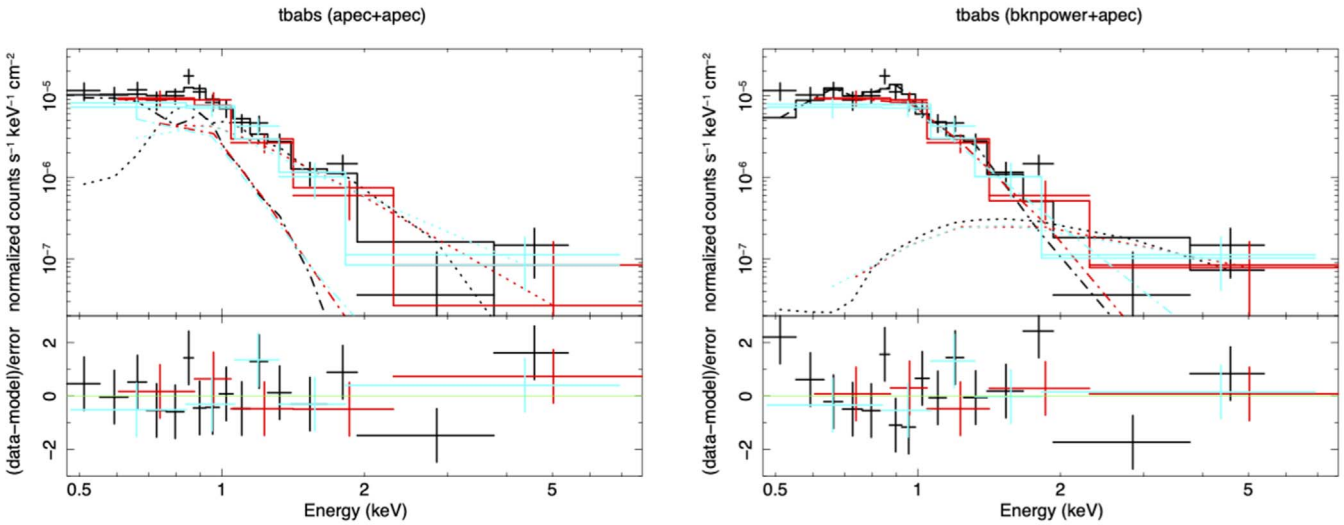

Figure 2. Fitting of all EPIC detectors (pn:black, MOS1:red, and MOS2:cyan) for the high-flux observation of δ Cepheid. Left: in the top panel, we show the integrated X-ray spectrum, along with the best-fitting folded model consisting of two absorbed APEC components (dashed–dotted line and dotted line respectively), and in the bottom panel, we show the fit residuals in terms of sigmas with error bars of size 1σ. Right: same as the left panel, but with the best-fitting folded model consisting of an absorbed APEC component (dashed–dotted line) and a power-law component (dotted line).

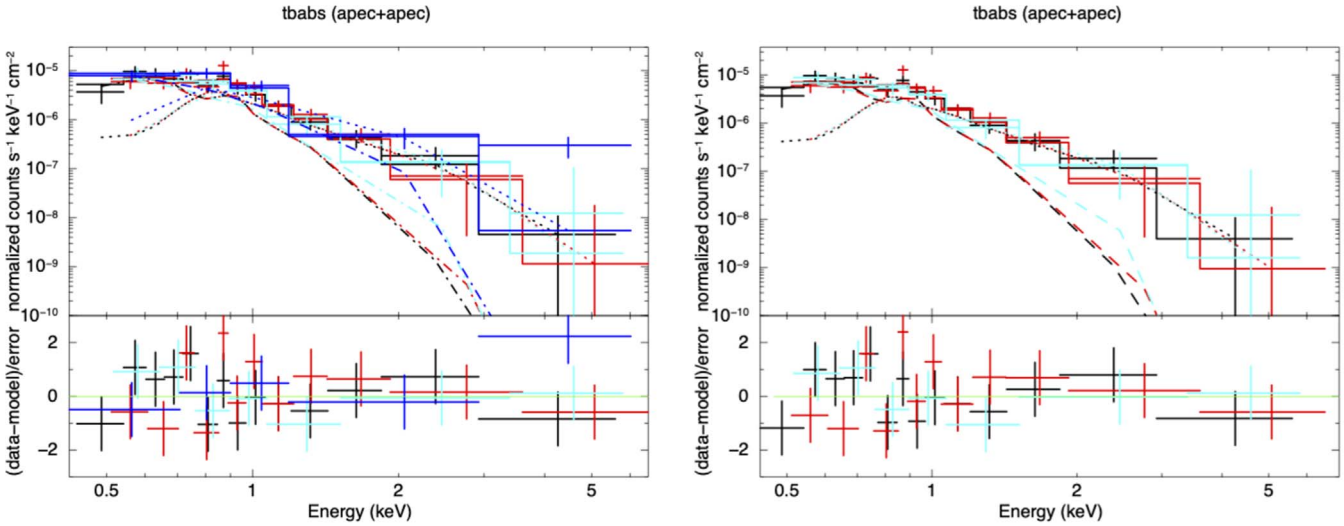

Figure 3. Fitting of all the low-flux pn observations shown in the colors black, red, cyan, and blue for OBSIDs 0723540301, 0723540401, 0603740901, and 0552410401, respectively. Left: on the top panel, we show the time-integrated X-ray spectrum, along with the best-fitting folded model comprised of two thermal absorbed APEC components (dashed–dotted line and dotted line). The bottom panel shows the fit residuals in terms of sigma with error bars of size 1σ. Right: same as the left panel, but excluding OBSID 0552410401 (blue data points).

2.3. Low-flux spectrum

The same fitting method as in the high-flux spectrum case was followed for the low-flux spectrum. In this case, we included only pn EPIC spectra of the four different low-flux observations (see Table 1) because in the MOS detectors the lower effective area leads to weaker signal that contributes less than three bins in each observation. In the left panel of Figure 3, we show the low-flux spectrum for all pn observations in different colors. We notice that observation 0552410401 (blue data points) appears to show a harder spectrum based on the single data point above 3 keV. In fact, this particular observation exhibits higher flux values when split into different phases, as shown by the green points in Figure 3 of Engle et al. (2017): at phase ∼0.4, during the rise phase, the flux is about 50% higher than the low-flux observations (yellow data points of Figure 3 therein). Moreover, given the same normalization of the spectral peak, the pn flux at 5 keV in the high flux (black points in Figure 3) is $\sim 10^{-7}$ ct/s keV cm^2 and in the low flux (Figure 3, right panel, excl. 0552410401) the pn flux is about 10 times smaller. Therefore, the observation 0552410401 is likely not to belong with the low-flux observations, since it shows harder spectrum and higher flux similar to that of the high-flux observation. For that reason, we performed separate spectral fits including and not including observation 0552410401.

The best-fit model for both cases (including OBSID 0552410401: $\chi^2_\nu = 1.12$, and excluding OBSID 0552410401: $\chi^2_\nu = 1.07$) is given by a two-component thermal plasma model (last two rows of Table 2). The left panel of Figure 3 shows the time-integrated spectra including OBSID 0552410401 (blue data points) and fitted with this two-component thermal model, while the right panel shows the same fit excluding OBSID

0552410401. The nonthermal electrons are expected to be cooling down in the low-flux interval, as shown by the timescale analysis in Section 3; thus, the power-law component is expected to be either reduced or suppressed in the low-flux spectrum relative to the high-flux one. We have performed spectral fits with a thermal+power-law component following the same logic as for the high-flux observation. By including OBSID 0552410401, a fit with a given $\Gamma = 2.0$ yields $\chi^2_\nu = 1.30$ while excluding it yields $\chi^2_\nu = 1.35$. From the best-fit models, we find that the contribution of the nonthermal flux to the energy-integrated source flux in the 0.3–10 keV band is similar to the high-flux case at ∼29% in the case where we include OBSID 0552410401, and ∼25% when OBSID 0552410401 is excluded.

Overall, the combined flux-spectrum analysis leads us to conclude that a nonthermal component, although not completely suppressed in the transition between the high- and low-flux state, is strongly reduced. A nonthermal contribution might harden the low-flux spectrum via OBSID 0552410401. However, because it contributes only one data point (∼5 keV) with relative large error in energy, its statistical significance does not allow us to firmly conclude that in the low-flux state the high-energy electron population has completely cooled.

3. Timescales for Thermal and Nonthermal Emission at Pulsation-driven Shocks

In this section, we compare the timescale of electron acceleration at the pulsation-driven shocks with the timescale of the radiative cooling and the nonthermal energy-loss processes relevant to relativistic electrons (Inverse Compton, synchrotron, bremsstrahlung, and Coulomb losses) under the constraint that these processes deplete the high-energy electron population on a timescale shorter than the pulsation period t_p. The timescale of each process is related, in each separate subsection, to the properties of the wind or the propagating shock and compared with t_p.

The thermal spectra shown in Section 2 reveal a shock-heated plasma at very high temperature far out from the star, much hotter than the typical effective temperature of a Cepheid ($T_{\rm eff} \sim 6000$ K). Moschou et al. (2020) concluded that Cepheids exhibit a two-component X-ray emission, with shock waves being responsible for the phase-dependent variable emission (phases 0.2–0.6) and with a separate mechanism being the dominant source of emission for the "quiescent" phases. In this scenario, the shock heating acts on this pre-existing hot plasma only in locally more rarefied wind regions.

A sudden thermal X-ray emission, distinct from the continuum X-ray emission, can be reconciled with a cold stellar wind only if a shock encounters a density inhomogeneity or undergoes strong time variability. This possibility is also consistent with the low surface flux of δ Cep combined with a fairly high temperature ∼1 keV, as emphasized by Engle et al. (2017), that might suggest an emission localized to a small angular region. We envisage the scenario (see Figure 4) of a stellar pulse that, in its expansion outward, encounters inhomogeneities in the circumstellar medium that slow down the pulse, whereas the regions of the pulse expanding unimpeded by inhomogeneities might steepen into shock waves and heat/ionize the medium. As the stellar pulsation continues, multiple shocks cross the same circumstellar region that, after the passage of a "first" shock, encounter a mostly ionized coronal plasma, instead of the quiescent δ Cep neutral wind. A nonspherical distribution of pulse velocity might also originate deeper in the stellar atmosphere, rather than being caused by the ambient medium. Cold (∼40 K) interstellar clouds detected in IR (70 and 160 μm) Herschel images around the Cepheids V Cen and RS Pup (Hocdé et al. 2020) observationally support the scenario shown in Figure 4.

Circumstellar envelopes (CSEs) around δ Cep (located at $2.4 \pm 0.1\,R_\star$), and the Cepheid Polaris, were detected in the near-infrared (NIR) band K' (1.9–2.3 μm) via interferometry techniques using the Fiber Link Unit for Optical Recombination (FLUOR) instrument at the Center for High Angular Resolution Astronomy (CHARA) array (Mérand et al. 2006); CSEs were also detected around other Cepheids in the IR (Kervella et al. 2006) and mid-IR (Gallenne et al. 2021), the latter for 13 stars (29% of their sample). The CSEs seem uncorrelated with the stellar mass loss, the temperature, or the presence of carbon monoxide (Gallenne et al. 2021), and they remain unexplained. Cold/hot dust composition of the CSE is ruled out by IR observations at 30 μm (Hocdé et al. 2020). A thin ($\sim 0.15\,R_\star$) shell of ionized gas was postulated (Hocdé et al. 2020) as the origin of the IR emission (for a sample of five Cepheids, not including δ-Cep), in agreement with an expanding Hα shell within the stellar atmosphere (Gillet 2014). The presence of ionized material within a few $R_\star$ and Hα profiles supports the scenario of shock waves driving the ionization of the circumstellar region proposed here (see Figure 4).

In relation to the expected periodicity, the level of precision of observations for δ-Cep and Polaris is insufficient for drawing conclusions on any asymmetry or time modulation of the CSE (Mérand et al. 2006); likewise, mid-IR excess, available only at a specific phase, does not lead to any time-dependence conclusion. However, the change in the IR atmospheric opacity at 4.6 μm due to the destruction-reformation cycle of carbon monoxide (Scowcroft et al. 2016) might be related to the stellar pulsation, and hence to the X-ray emission from electrons accelerated at shock waves that ionize the CSE in their outward propagation.

3.1. Radiative Cooling

The X-ray spectral fit shown in Section 2 is consistent with a gas shock-heated to a temperature $T_{\rm sh} \simeq 3 \times 10^6$ K from a shock wave traveling at a few hundred km s^{-1}: from the jump conditions, the post-shock temperature scales as $T_{\rm sh} = 3 m_p \mu V_{\rm sh}^2/16k \sim 1.5 \times 10^6 K\,(V_{\rm sh}/(300{\rm km\ s^{-1}}))^2$, where $V_{\rm sh}$ is the shock speed in the local upstream frame and the mean atomic mass in units of proton mass is benchmarked at $\mu = 1$. The X-ray lightcurve constrains the shock-heated gas radiative cooling time to be shorter than the pulsation period.

The pristine and predominantly neutral wind gas of a Cepheid star is continuously ionized in local regions by traveling shocks, on a timescale very rapid compared with the wind expansion timescale. Therefore, the ion density encountered by subsequent shocks passing through a post-shock region is much larger than the ion density in unshocked regions, due to the freshly ionized neutrals and can be approximated with the pre-shock neutral density : $n_i^{\rm sh} \sim n_{\rm H}$. Thus, the source of the X-ray emission rarefies outward as R^{-2}. Moschou et al. (2020) used 1D radial wind density profiles for various mass-loss rates and determined the location R of the X-ray source by intersecting these profiles with the value of the

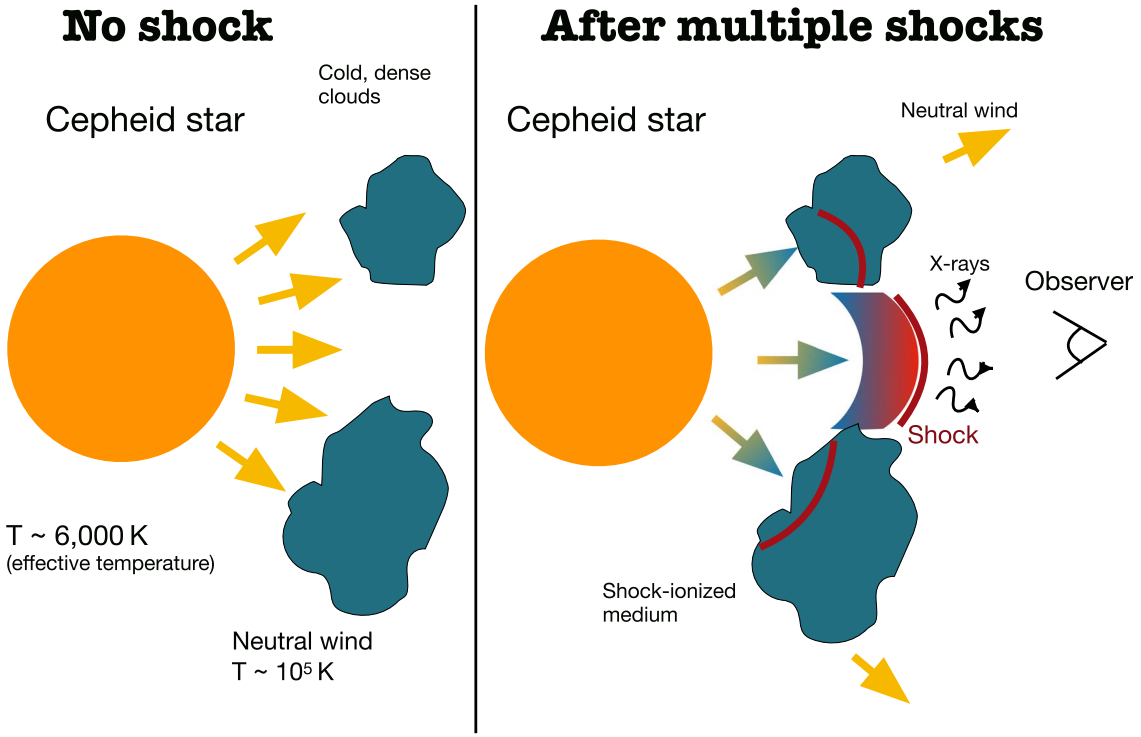

Figure 4. Cartoon illustration of the pulsation-driven shocks propagating into the pre-ionized circumstellar medium.

density needed for a radiative cooling time of 12 hr, to match the decay of the X-ray peak (see the lower panel of Figure 7 therein). Here, we allow for a 3D distribution of cold partially neutral clumpy circumstellar medium that slows down shocks and a highly ionized medium heated up by shocks that radiatively cools on a timescale shorter than t_p and that supplies the electrons accelerated by the shocks.

The cooling via collisional excitation of heavy ions by electrons has been calculated for the optically thin highly ionized plasma in the solar corona by, e.g., Landi & Landini (1999) and Colgan et al. (2008), and it can be approximated for temperatures in the range $10^6 < T < 10^7$ K by $\Lambda(n_i, T) = n_i n_{\rm H}\ \tilde{\Lambda}(n_i, T_{\rm sh}) = n_i n_{\rm H}\ 10^{-23}$ erg cm^{-3} s^{-1}, where $\Lambda(n_i, T)$ is the cooling function, $\tilde{\Lambda}(n_i, T_{\rm sh})$ is the radiative power per unit of volume (or radiative loss), and the global neutrality condition is assumed ($n_e \sim n_i$). In the case of OB supergiants (Chen & White 1991a), the pre-shock wind is mostly ionized, with an average ion mass loss comparable with the neutrals' mass loss in Cepheids ($10^{-6}\,M_\odot$ yr^{-1}).

The ion-to-neutral fraction in the unshocked wind of δ Cep is uncertain, but expected to be small due to the low effective temperature. However, the gas cooling is highest in the post-shock region, freshly ionized by the passage of the shock. Thus, the neutral gas behind the shock is assumed to be entirely ionized, with a resulting n_i much greater than in the pre-shock gas. The neutral mass-loss rate was estimated from 21 cm line measurements of neutral hydrogen from circumstellar nebulae to be[3] $\dot{M} \sim 10^{-6}\,M_\odot$ yr^{-1} (Matthews et al. 2012). Fourier decomposition of the wind speed in the numerical simulations by Moschou et al. (2020) shows that, at a radius $3\,R_\star$, speed fluctuations in the acceleration region settle further out ($R > 10\,R_\star$) to a coasting speed $\sim$100 km s^{-1}; only the post-shock region very close to the shock cools radiatively. Thus, the maximal speed $\sim$100 km s^{-1} in the wind can be used to estimate the wind density in the shock region as follows. For the parameters listed above, the steady and optically thin mass loss corresponds to a neutral hydrogen number density

$$n_i(3\,R_\star) \simeq n_{\rm H}(3\,R_\star) = \frac{\dot{M}}{4\pi R^2 V(3\,R_\star) m\mu} = 4.46 \times 10^9 {\rm cm}^{-3} \times \frac{\dot{M}}{10^{-6}\,M_\odot\,yr^{-1}} \frac{100\ {\rm km\ s}^{-1}}{V} \times \left(\frac{8.4 \times 10^{12}\ {\rm cm}}{R}\right)^2, \quad (1)$$

where $R_\star = 40 R_\odot = 2.8 \times 10^{12}$ cm. The cooling timescale in the post-shock region is strongly reduced (with respect to the ion density in the unshocked wind), and at a distance R from the star it is

$$t_{\rm rad}(R) \simeq \frac{3\,n_i(R)\,k_B T_{\rm sh}}{2\,\Lambda(n_i, T_{\rm sh})} \simeq 0.72\ {\rm d} \frac{T_{\rm sh}}{3 \times 10^6 K} \frac{10^9 {\rm cm}^{-3}}{n_{\rm H}(3\,R_\star)} \frac{10^{-23} {\rm erg\ cm^3\ s^{-1}}}{\tilde{\Lambda}(n_i, T_{\rm sh})} \left(\frac{R}{3\,R_\star}\right)^2, \quad (2)$$

where the scaling $n_{\rm H} \sim R^{-2}$ accounts for the coronal rarefaction and we have used $n_{\rm H} \simeq n_i$. Because the plasma continues its acceleration outward (Moschou et al. 2020), the post-shock temperature is not appreciably decreased by the cooling.

[3] For an optically thin wind of giants and supergiants in the spectral range G0–M5 (Drake & Linsky 1986), an upper limit to the steady time-averaged mass-loss rate of the ionized component of the wind is $3.2 \times 10^{-10} M_\odot$ yr^{-1}, assuming an outflow speed of 35 km s^{-1} (below the escape speed), $T = 10^4$ K, and $R = 41.6 R_\odot$. Lower surface temperature or wind speed lead to a lower mass-loss rate. This mass-loss rate corresponds to a much smaller steady-state ion density ($\sim 10^6$ cm^{-3}).

A comparison of $t_{\rm rad}$ with $t_p \sim 5$ d (see Figure 5) shows that, depending on several wind parameters, between $3\,R_\star$ and $10\,R_\star$ from the star, the pulsation outruns the radiative cooling as $t_{\rm rad}$ grows from $t_{\rm rad}(3\,R_\star) \sim 0.72$ days to $t_{\rm rad}(10\,R_\star) \sim 7$ days $> t_p$, due to the wind rarefaction, and the radiative cooling is suppressed at $10\,R_\star$. This rise of $t_{\rm rad}$ provides a constraint on the location R of the thermally emitting region in the δ Cep corona, although this condition remains uncertain due both to several poorly determined observational parameters, e.g., neutral and ion wind densities, and empirical models for the radiative cooling. Because the cooling of the post-shock region slows down as the shock moves outward, a larger fraction of the shock ram pressure can be transferred to electrons that can be heated/accelerated.

We have assumed that both the thermal and nonthermal X-ray emission (Engle et al. 2017) originate in the shock-heated plasma ($T_{\rm sh} \sim 3 \times 10^6$ K). Moschou et al. (2020) did not restrict the radiative cooling to the post-shock region, and they determined the radiative cooling time by using two likely average coronal plasma temperatures, both much colder than the post-shock plasma (for 18 out of 20 cases, $T \sim 5 \times 10^5$ K; see Table 1 therein), that also adiabatically decrease ($T(r)$), thereby reducing $t_{\rm rad}(R)$ by a factor $\sim$6. At temperatures 10^5–10^6 K , the $\tilde{\Lambda}(n_i, T_{\rm sh})$ is about 100 times larger than at 10^7 K (Landi & Landini 1999; Colgan et al. 2008; Moschou et al. 2020), thereby greatly suppressing the radiative cooling timescale,[4] before it adiabatically cools outward into the range 10^4–10^5 K, where $\tilde{\Lambda}(n_i, T_{\rm sh})$ is only $\sim$10 times larger than at 10^7 K.

An opposite effect that increases $t_{\rm rad}$ in the simulations by Moschou et al. (2020) with respect to Equation (2) above is the large wind speed. In the dense coronal plasma, the shock layer, if estimated through the ion inertial length as heliospheric interplanetary shocks indicate, is remarkably thin: $c/\omega_{pi}(3\,R_\star) \sim 10^3$ cm $\sqrt{10^9\ {\rm cm^{-3}}/n_i^s(3\,R_\star)}$, far shorter than the shock spacing, with a $t_p \sim 5$ days and speed $\sim$100 km s^{-1} (these values lead to a shock spacing $\sim 4 \times 10^{12}$ cm); the shock transition layer is much thinner than any other scale involved in the system, including the compressed post-shock plasma region as found in the simulations by Moschou et al. (2020). The maximal speed reached in the region behind each shock (within thickness $\sim 10^{12}$ cm; see Figures 3 and 5 in Moschou et al. (2020)) is $\lesssim$200 km s^{-1}, which leads to a smaller $n_{\rm H}$ (see Equation (1)) and a larger $t_{\rm rad}$. However, this effect is at most on the order of a few, whereas the decrease in $t_{\rm rad}$ due to the temperature $T_{\rm sh}$ can be as large as a factor of 10, hence the very small $t_{\rm rad}$ in Moschou et al. (2020).

3.2. Electron Acceleration at Pulsation-driven Shocks

We propose that the X-ray enhancement is powered by relativistic electrons accelerated at the shocks propagating out in the stellar corona. Generally, a higher acceleration rate at nonrelativistic shocks is realized by a higher shock speed, a stronger magnetic field B, or a magnetically oblique shock (Jokipii 1982; Drury 1983). Due to the rapid drop of the magnetic field with the radial distance from the star, i.e., $B \simeq R^{-3}$ (see below in this subsection the dipolar field assumption), the acceleration rate declines rapidly outward from the star, thereby constraining X-ray emissions on scales shorter than t_p to regions very close to the star, i.e., within $10\,R_\star$.

Electron acceleration at the propagating shock can be sustained diffusively up to large energies if the particle–particle collision mean free path is far greater than the hydrodynamical scale of the system. For fast electrons, the electron–ion collision frequency (much greater than the electron–electron collision frequency) scales as $\nu_{ei} \sim 10^{-9}\ n_i Z^2 \Lambda_{ei} E[{\rm eV}]^{-3/2}$. For a 10 keV electron, this leads to a collision mean free path within the shocked pre-ionized dense stellar corona of

$$\lambda_{ei} = 3\,\frac{v}{\nu_{ei}} \simeq 10^{15}\ {\rm cm}\frac{10^9\ {\rm cm^{-3}}}{n_i} \tag{3}$$

(where v is the electron speed and we have used $\Lambda_{ei} \sim 20$) that largely exceeds all other length scales for the outward-propagating shock, ensuring that the collisionless regime holds throughout the electron energy spectrum.

The population of shock-accelerated electrons (>10 keV) is pitch-angle isotropic in the local upstream plasma rest frame, due to the very high particle speed compared with the shock speed ($\sim$100 km s^{-1}); thus, the scaling for the diffusive shock acceleration applies (Drury 1983). Particle escape from the shock, competing with the acceleration and leading to a cutoff or no-power-law energy spectrum (Fraschetti 2021), or effects due to radial expansion (Drury 2011) are neglected herein; energy losses are detailed in Section 3.3. The acceleration timescale, $t_{\rm acc}$, for an electron of Lorentz factor γ at a shock moving with speed C_r in the stellar wind frame[5] with an embedded magnetic field $B = |\boldsymbol{B}|$ can be approximated by (Parizot et al. 2006; Fraschetti et al. 2018)

$$\begin{aligned} t_{\rm acc}(\gamma) &\simeq 1.83\frac{3r^2}{r-1}\frac{D_0(\gamma)}{C_r^2} \\ &= 2.4 \times 10^{-4} d\ \frac{r^2 k_0}{r-1}\ \frac{0.01G}{B(3\,R_\star)} \\ &\quad \times \left(\frac{200{\rm km\ s^{-1}}}{C_r(R)}\right)^2 \frac{\gamma^2-1}{\gamma}\left(\frac{R}{3\,R_\star}\right)^3, \end{aligned} \tag{4}$$

where r is the density compression at the shock, $D_0(\gamma)$ is the spatial diffusion coefficient for an isotropic upstream turbulence, and $k_0 = D_0/D_B$, assumed to be equal upstream and downstream (Parizot et al. 2006), where D_B is the Bohm diffusion coefficient at the electron Lorentz factor γ.

As described by Chen & White (1991a), the background plasma in the post-shock region might loses most of its energy via radiative cooling, until the dominant pressure terms become the magnetic or the nonthermal pressures. The nonthermal energy content at Mach number shocks <10 is typically <15% of the total downstream energy (and of the upstream ram pressure) and it does not depend on the shock magnetic obliquity (i.e., angle between the upstream magnetic field and the normal to the shock surface), as an accurate analysis of in situ measurements of interplanetary shocks found (David et al. 2022). However, nova V745 Sco outbursts show a significant drop in plasma temperature within $\sim$10 days,

[4] At such high temperatures ($\gg 10^4$ K), recombination of the gas is not efficient.

[5] For an expected stellar wind speed $\sim$30 km s^{-1} within $10\,R_\star$, much smaller than the numerically determined shock speed ($\sim$a few hundreds of km s^{-1} at a distance of $3\,R_\star$, from Moschou et al. 2020), we can approximate C_r to be equal to the speed in the stellar frame.

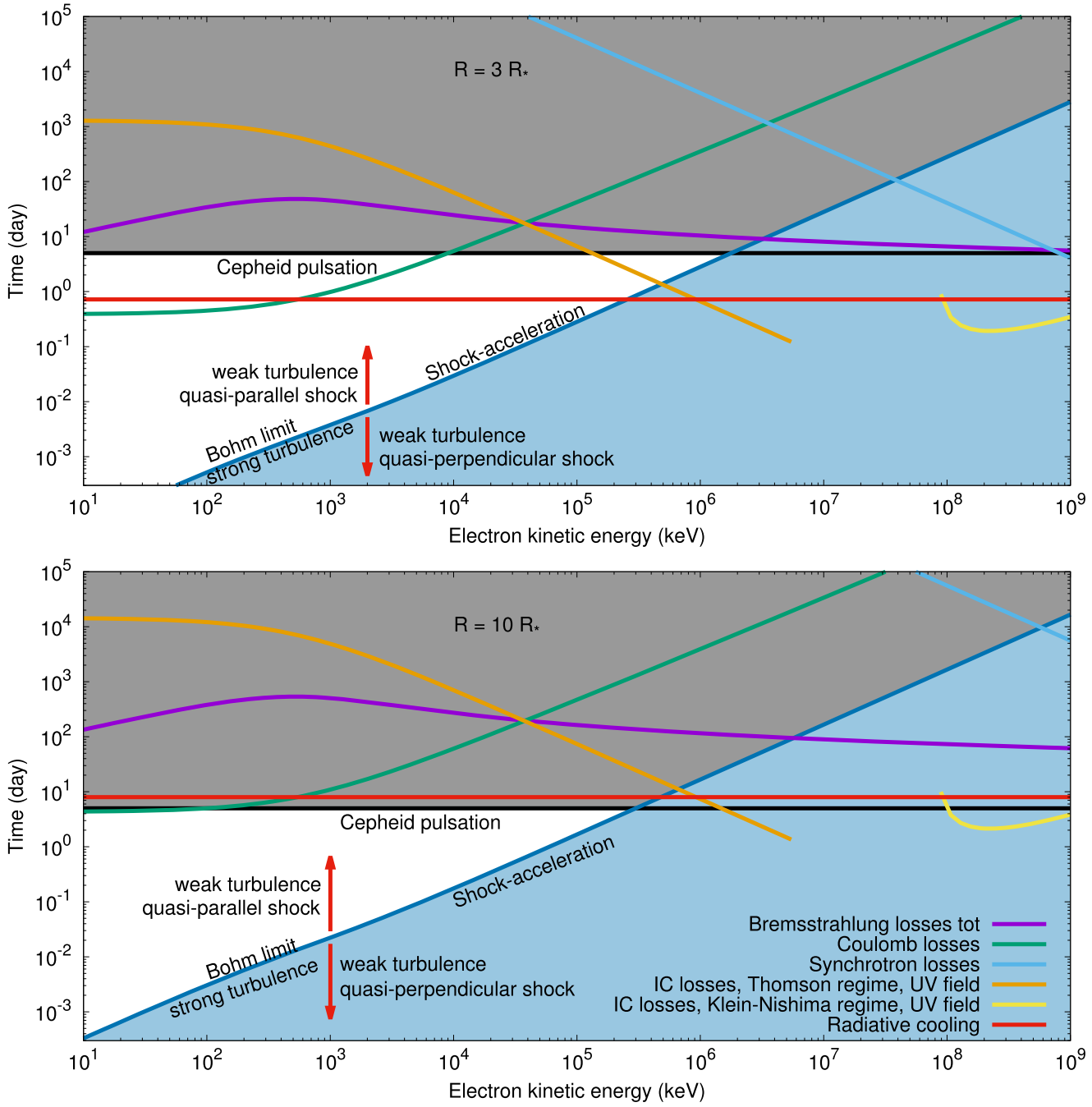

Figure 5. For energetic electrons accelerated at a shock (density compression $r = 4$) traveling through the stellar corona, the timescales for the nonthermal energy losses (bremsstrahlung $t_{\rm brem}$, IC $t_{\rm IC}^{T}$ and $t_{\rm IC}^{\rm KN}$, Coulomb $t_{\rm Cou}$, and synchrotron $t_{\rm syn}$), nonradiative shock acceleration $t_{\rm acc}$ (in blue Bohm regime, or strong magnetic turbulence, i.e., $k_0 = 1$) and thermal radiative cooling $t_{\rm rad}$ are compared with the estimated δ Cep pulsation period. The Bremsstrahlung timescale includes both e-e and e-p collisions (Haug 2004, Equation (9) therein). The shaded blue (blank) area below (above) the blue curve corresponds to the case $k_0 < 1$ ($k_0 > 1$), i.e., weak turbulence at quasi-perpendicular (quasi-parallel) magnetic obliquity. The gray shaded area above the black line corresponds to times longer than t_p (black horizontal line), which are thus ruled out by X-ray observations. Top: $R = 3\ R_\star$, with shock speed $C_r = 200$ km s^{-1} (Moschou et al. 2020), $n_i(3\ R_\star) = 10^9$ cm^{-3}, $n_{\rm H}(3\ R_\star) = 10^9$ cm^{-3}, and $B(3\ R_\star) = 0.01$ G. Bottom: Same as top panel, but with $R = 10\ R_\star$, a shock speed $C_r = 500$ km s^{-1}, and scaling of n, $n_{\rm H}$, and B as described in Section 3.3.

possibly due to a nonthermal energy content as large as 50% (Drake et al. 2016). The compression experienced by the energized electrons is larger at larger energies, as the latter travel greater distances from the shock. The average displacement during $\Delta t \simeq 1$ day of a 1 GeV electron diffusing around the shock can be as large as $\Delta x \sim \sqrt{2\, D_B \Delta t} \simeq 10^{11}$ cm, much greater than the presumed shock thickness $\sim c/\omega_{pi}(3\ R_\star) \sim 10^3$ cm. As a consequence, if the shock enters the radiative regime, the shock compression acquires a dependence on the particle energy and the estimate of $t_{\rm acc}$ needs a correction beyond the scope of this paper.

As for the turbulence effect in the shocked region, the acceleration timescale varies considerably according to the geometry of the upstream magnetic field $\boldsymbol{B}$, i.e., if $\boldsymbol{B}$ is parallel or perpendicular to the shock normal (see Figure 5). In the weak turbulence regime (far from Bohm regime), it holds that $k_0 \gg 1$ ($k_0 \ll 1$) for shocks in quasi-parallel (or quasi-perpendicular) geometry (e.g., Fraschetti & Giacalone 2012);

for strong turbulence, the total (average + turbulent) magnetic field is nearly isotropic in configuration space because the turbulence becomes dominant, leading to the Bohm regime ($k_0 \simeq 1$; blue curve in Figure 5). For a quasi-perpendicular shock, the acceleration rate has been long known to be higher hence a faster particle energization (Jokipii 1982, 1987; Giacalone 2005; Fraschetti & Giacalone 2015), namely $t_{\rm acc}$ shorter ($k_0 < 1$, see Figure 5). Figure 5 depicts the acceleration timescale as a function of electron kinetic energy for the case $k_0 = 1$ (blue curve). The blue shaded (blank) region is accessible to quasi-perpendicular (quasi-parallel) shock geometry by varying k_0 ; electrons can reach kinetic energy >1 GeV at a quasi-perpendicular shock before the cooling dominates, according to loss processes described in Section 3.3.

In Equation (4), the ambient magnetic field strength is assumed to be dominated by the dipolar component, hence the scaling $B \simeq R^{-3}$ with the choice $B(3\,R_\star) = 0.01$ G, which corresponds to the average surface magnetic field 0.43 G inferred in a single spectropolarimetric observation with ESPaDOnS by Barron et al. (2022). This magnetic field squeezes the region of particle acceleration close to the star before losses outpace acceleration, in contrast with the $B \simeq R^{-2}$ scaling in Chen & White (1991a), where the acceleration time increases at a slower rate with the radial distance. A dominant monopole scaling $B \sim R^{-2}$ instead of the dipole used here would not change the conclusion in Figure 5.

Hydrodynamic simulations (Moschou et al. 2020) show that the Mach number of the traveling compressions in the local plasma frame, approximately coinciding with the stellar frame as the quiescent wind speed is only $\sim$30 km s^{-1}, spans the range 1–10 very close to the star surface ($\sim 2\,R_\star$) and keeps increasing out to $\sim 40\,R_\star$. In a circumstellar medium with magnetic field $B(3\,R_\star) \sim 0.01$ G and ion density $n_i = 10^9$ cm^{-3} (the models of spanned values of ion number density between 10^6 and 10^9 cm^{-3} (Moschou et al. (2020)), the Alfvén speed is $\sim$1 km s^{-1}, much smaller than the local sound speed $\sim$500 km s^{-1} at the shock-heated regions (Moschou et al. 2020). Thus, the expected spectral slope of energized electron is approximately determined by the sonic Mach number radial profile as calculated in Moschou et al. (2020), and no correction due to the magnetic field introduced herein is needed.

Moreover, the hydrodynamic simulations in Moschou et al. (2020) suggest an increasing shock speed $C_r(R)$ during the first phase of the shock propagation. Guided by these simulations, in the two snapshots of Figure 5 calculated at $R = 3$ and $10\,R_\star$, we assigned to C_r the two values 200–400 km s^{-1} and compared $t_{\rm acc}$ with the losses timescales described in the following section at these two locations. Further out, the decrease of the $B-$field with radius reduces the efficiency of the shock acceleration so that, at a given electron energy, losses prevail outward. In addition, the shock speed in the local plasma wind frame depends on the assumed stellar neutral mass loss, which is highly uncertain.

3.3. Energy Losses in the Leptonic Scenario

In this section, we consider various processes of energy loss for the relativistic electrons accelerated as described in Section 3.2 to a Lorentz factor γ by a single pulsation-driven shock and compare the rates of energy loss with the acceleration timescale $t_{\rm acc}$, the thermal radiative cooling timescale $t_{\rm rad}$ and the stellar pulsation period t_p. Nonthermal emission is an unambiguous signature of the presence of relativistic electrons that can be transported far into the outer corona only by traveling shocks.

The energy-loss timescales increase rapidly with the distance R and exceed t_p only within a few stellar radii from the Cepheid star; however, losses can balance $t_{\rm acc}$ only after the time necessary for the shock to energize the electrons up to the $\sim$GeV range. Time-dependent effects on the electron energy spectrum due to the continuous process of acceleration and energy loss are neglected here.

3.3.1. Inverse Compton Scattering

We propose that the nonthermal enhanced X-ray emission in $\delta-$Cep originates from UV ($\sim$1–100 eV) stellar wind photons upscattered into X-ray band by the IC over the shock-accelerated electrons, as proposed by Chen & White (1991a) for OB supergiants. The target UV photon population within the photosphere/corona is assumed to be isotropic in the frame of the plasma flowing downstream of the shock, i.e., the Doppler effect is negligible for a shock speed $C_r \simeq 200$ km s^{-1}. The population of shock-accelerated electrons is also isotropic in the plasma frame at that shock speed, as pointed out in Section 3.2.

In the Thomson limit ($4\varepsilon_0\gamma/m_e c^2 \ll 1$, where $\varepsilon_0 = 5$ eV is assumed as the UV initial photon energy), the power $P_{\rm IC}^T$ emitted by a single electron is

$$P_{\rm IC}^T = \frac{4}{3}\sigma_T c \gamma^2\, U_{\rm rad}, \tag{5}$$

where $U_{\rm rad}$ is the photon energy density integrated over all frequencies, σ_T is the Thomson cross section, and c the speed of light in vacuum. The IC loss timescale in the Thomson limit at distance R from the stellar surface, using Equation (5), is

$$t_{\rm IC}^T(\gamma) = \frac{m_e c^2 \gamma}{P_{\rm IC}^T}\left(\frac{R}{R_\star}\right)^2 = \frac{1.3\times 10^3\ {\rm d}}{\gamma}\left(\frac{6000\ K}{T_\star}\right)^4\left(\frac{R}{3R_\star}\right)^2. \tag{6}$$

where we have used for the δ Cep stellar surface temperature $T_\star \sim 6000$ K and $U_{\rm rad} = \sigma T_\star^4/c$, where σ is the Stefan–Boltzmann constant, and the factor $(R/R_\star)^2$ accounts for the scaling of $U_{\rm rad}$. The decrease of $t_{\rm IC}^T(\gamma)$ with the electron kinetic energy is shown by the orange curve in both panels of Figure 5. This curve intersects $t_{\rm acc}$ and t_p (black line) at the smallest energy (GeV), making it the most efficient loss process.

It is noteworthy that, although the X-ray nonthermal IC emission in this scenario is assumed to originate from the same source as the thermal emission (shock region), the IC can be emitted by the energetic electrons escaped upstream from the shock, as well as those advected downstream of the shock, and interacting with the cool UV stellar wind photons (6000 K). The scenario by Chen & White (1991a) for OB supergiants also assumed that the sources of nonthermal/thermal emission are spatially coincident. However, the stellar wind in Chen & White (1991a) is assumed to be isothermal in the circumstellar region traveled by the shocks, in contrast with the radial scaling

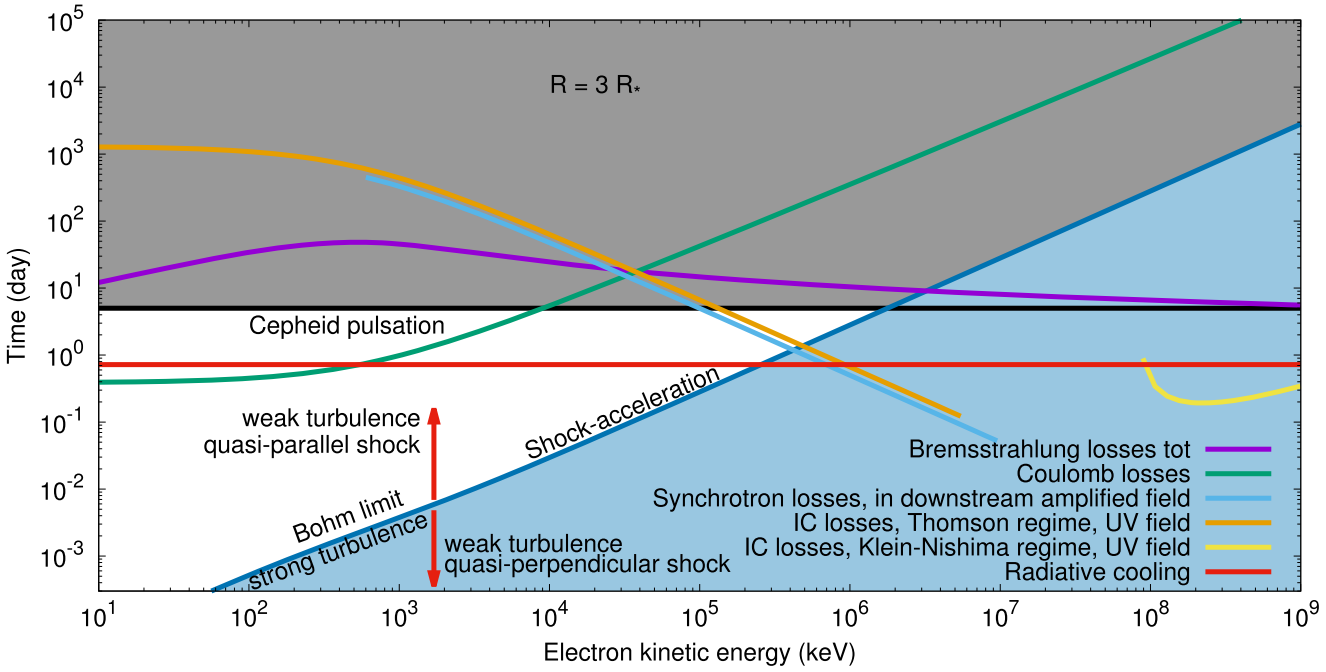

Figure 6. Same as Figure 5, but with an amplified magnetic field $\delta B = 300\, B(3\, R_\star) = 3$ G.

of the photon energy density $U_{\rm rad}$, i.e., of the temperature, assumed here.

In the extreme Klein–Nishima limit ($4\varepsilon_0\gamma/m_ec^2 \gg 1$), for the monochromatic target photon field, the power $P_{\rm IC}^{KN}$ emitted by a single electron is given by (Schlickeiser 2009; Fraschetti & Pohl 2017)

$$P_{\rm IC}^{\rm KN} \simeq \frac{3}{8}\sigma_T\, c (mc^2)^2 \frac{n_0}{\varepsilon_0}\left[\ln\frac{4\varepsilon_0\gamma}{m_ec^2} - \frac{11}{6}\right], \tag{7}$$

where we have used $n_0 = \sigma T_\star^4/c\ \varepsilon_0$. The IC loss timescale, using Equation (7), is

$$t_{\rm IC}^{\rm KN}(\gamma) = \frac{m_ec^2\gamma}{P_{\rm IC}^{\rm KN}}\left(\frac{R}{R_\star}\right)^2 = \frac{\gamma}{\frac{3}{8}\sigma_T mc^3\frac{n_0}{\varepsilon_0}\left[\ln\frac{4\varepsilon_0\gamma}{m_ec^2} - \frac{11}{6}\right]}\left(\frac{R}{R_\star}\right)^2$$
$$= 4.5 \times 10^{-7} d\ \frac{\gamma}{\left[\ln[3.9\times 10^{-5}\gamma] - \frac{11}{6}\right]}$$
$$\left(\frac{6000\ K}{T_\star}\right)^4\left(\frac{R}{3R_\star}\right)^2. \tag{8}$$

Figure 5 shows that the IC losses in the KN regime are ruled out due to an electron energy cutoff at energies too low at $R = 3\, R_\star$ for the KN regime.

3.3.2. Synchrotron Losses

The relativistic electrons also undergo synchrotron loss at the shock, which might contribute to the nonthermal emission. Assuming spatial 3D isotropy of the upstream magnetic field B, the magnetic strength is compressed downstream to $0.83\, r\, B$, where the factor 0.83 is due to the upstream isotropy (Parizot et al. 2006). The synchrotron loss timescale can be written as

$$t_{\rm syn}(\gamma) = \frac{10^8 d}{\gamma}\left(\frac{0.01G}{0.83\ r\ B(3\ R_\star)}\right)^2\left(\frac{R}{3\ R_\star}\right)^6. \tag{9}$$

Figure 5 shows that, for $B(3\, R_\star) = 0.01$ G, the synchrotron timescale becomes comparable with t_p only in the $E \sim$ TeV energy range and close-in ($\sim 3R_\star$). If the magnetic field is locally much stronger both upstream and downstream (due to, e.g., plasma instabilities), for example, $B(3\, R_\star) = 1$ G (Figure 6), the Alfvén speed becomes comparable with the sound speed, thereby reducing the Mach number, and synchrotron cooling dominates over the IC cooling off the UV stellar field. However, in such a large upstream B-field, the acceleration rate is also enhanced and the electron energy cutoff, due to synchrotron cooling, increases to $\sim$5 GeV, higher than in the IC-dominated case.

Another possible scenario of enhanced B is based on X-ray emission from the clumps, heated by the shocks, that are likely to cover a broad range of spatial scales within the inner corona. Such inhomogeneities can trigger an amplification of the magnetic field downstream of the shock due to vorticity generation, as first demonstrated in MHD simulations by Giacalone & Jokipii (2007) and Inoue et al. (2012) and analytically described in terms of structure of upstream clumpiness by Fraschetti (2013). In the latter model, the B-saturation strength depends on the radius R_c of the clumps and on the thickness ℓ_F of the outer layer where the gas density gradient is nonvanishing (Fraschetti 2013); if $\ell_F/C_r \ll 1$ day, the amplified downstream magnetic field can saturate at a turbulent strength δB far higher than the seed field $B(3\, R_\star)$, consistently with the δ-Cep observations. Such an amplification process has been suggested (Fraschetti et al. 2018) to explain time variability of X-ray flux at the Cas-A supernova remnant (Sato et al. 2018). The saturation turbulent field scales with the shock Alfvén Mach number M_A as $\delta B/B(3\ R_\star) \simeq M_A\sqrt{2\ R_c/\ell_F}$ (Fraschetti 2013). For $M_A \sim 30$ and $R_c/\ell_F \sim 50$, the magnetic

field is ∼300-fold enhanced and the synchrotron cooling overruns the IC cooling of the UV stellar field (see Figure 6):

$$t'_{\rm syn}(\gamma) = \frac{7.3 \times 10^6 d}{\gamma}\left(\frac{1G}{\delta B}\right)^2\left(\frac{R}{3R_\star}\right)^6. \quad (10)$$

It is noteworthy that, if the B-field amplification is caused by medium inhomogeneity, the synchrotron cooling time is shortened, whereas the acceleration timescale, which depends on the upstream field, is unchanged.

3.3.3. Bremsstrahlung

In the dense coronal environment, even in the shock-compressed region, the density of ions generated by the ionization from the passage of a previous shock is at most of order $n_i(3R_\star) \sim 10^9$ cm^{-3} (see discussion above). In such a high-density environment, the bremsstrahlung energy-loss timescale due to collision of the energetic electrons of kinetic energy E with thermal protons in a fully ionized hydrogen plasma or with thermal electrons is given by (Equations 7–9 of Haug 2004)

$$-\left(\frac{dE}{dt}\right)_{\rm brem} = m_e c^3\, n_i\left(\alpha\,\frac{3}{8\pi}\sigma_T\,\frac{8\gamma^2}{\gamma^2-p^2}A_p(E) + A_e(E)\right),$$
$$t_{\rm brem}(E) = \left(\frac{1}{E}\frac{dE}{dt_{\rm brem}}\right)^{-1}\left(\frac{R}{R_\star}\right)^2, \quad (11)$$

where $p = \sqrt{\gamma^2-1}$ and the factors $A_p(E)$ and $A_e(E)$ describing the target particle, proton and electron, respectively, are defined in the Appendix.

In Equation (11), we have neglected admixtures of heavier ions and considered only electron–proton bremsstrahlung. Figure 5 shows that for the ion number density expected in the stellar corona $t_{\rm brem} \gg t_p$ within the kinetic energy range (1–10^9) keV both at distance 3 and $10R_\star$ from the star; thus, denser plasma regions in the inner corona cannot power bremsstrahlung emission at a sufficiently high rate to explain the X-ray enhancement (Engle et al. 2017). In the tenuous outer stellar wind regions (with shock-generated ion density $n_i \sim R^{-2}$; see Moschou et al. 2020), the bremsstrahlung loss rate for the accelerated electrons decays as the shock travels outward in the stellar corona. Only in an extremely dense wind ($n_{\rm H} \sim 10^{10}$ cm^{-3}) can bremsstrahlung emission exceed the IC. However, such large plasma density also suppresses the radiative cooling timescale to only a few tens of minutes and the particle acceleration in a much cooler, denser, and more unstable downstream condition might not proceed adiabatically.

3.3.4. Coulomb Losses

Although a shock ionizes most of the stellar wind gas that it encounters, subsequent shocks are likely to encounter a comparable neutral component. Thus, the rate of energy loss in the ionization of neutral hydrogen should be considered as well. The timescale for Coulomb losses can be expressed as (Longair 1994, Equation (19.1))

$$t_{\rm Cou}(\gamma) \simeq 7.5 \times 10^2\, d\,\frac{\gamma}{3\ln\gamma + 19.8}\,\frac{10^9\ {\rm cm}^{-3}}{n_{\rm H}(3\,R_\star)}\left(\frac{R}{3R_\star}\right)^2. \quad (12)$$

The Coulomb timescale is shown (in Figures 5 and 6, depicted in green) to exceed all others listed above in the energy range of interest.

4. Discussion

4.1. X-Ray High- and Low-flux State Relation with the UV Flux

The observations of the X-ray enhancement in $\delta-$Cep are consistent with a physical model that combines a single thermal with a nonthermal component that cools on a timescale comparable with the stellar pulsation period. The observations analyzed herein do not rule out that a nonthermal component might still be present during the low-flux interval and did not completely dissipate during the high-flux one, despite being largely reduced. The rate of ejection of the shocks heating the plasma in the rarefied regions might be too high for the nonthermal population to cool completely, as illustrated in Figure 5. On the other hand, a two-temperature model, similar to the one used in Engle et al. (2017), provides a good fit with no need of a nonthermal component; however, the origin of the two distinct temperatures remains to be determined.

The X-ray enhancement is observed during the phase of maximum angular radius—whereas, based on photospheric observations, this particular phase of pulsation is rather quiet. Evidence of shocks from the far-UV peak is collected (Engle et al. 2017) on the ascending branch of the lightcurve, immediately after the radius minimum, e.g., ∼2.7 days before the X-ray enhancement. Such a delay of a fraction of t_p suggests that the radiative cooling occurs earlier within the pulsation period than the IC cooling of the accelerated electrons; we find a comparable delay in Figure 5 (top panel) at $R = 3\,R_\star$ between $t_{\rm rad}$ (red curve) and the IC cooling condition $t_{\rm acc} = t^T_{\rm IC}$, denoted by the intersection of the blue and orange curves. Our timescale estimate shows that this process is constrained to occur within $10\,R_\star$ (see Figure 5, bottom panel), and that the distance of $3\,R_\star$, close to the ionized shell postulated by Hocdé et al. (2020), is consistent with the observed delay between X-ray flash and FUV peak.

The scenario proposed here of an IC emissivity off the stellar UV background to generate the nonthermal component and radiative cooling from the shock-heated gas to produce thermal emission is consistent with the expected parameters for star and circumstellar medium. We discuss below some implications of the nonthermal scenario and mention a support from VLA radio counterpart.

4.2. Energetic Electron Cutoff

A comparison of $t_{\rm acc}$ with $t^T_{\rm IC}$ and $t_{\rm rad}$ in Figure 5 (blue, orange, and red, respectively), shows that, due to the short radiative cooling time (∼a few days), the post-shock plasma approaches a radiative regime roughly at the same energy scale of the crossing of $t_{\rm acc}$ with $t^T_{\rm IC}$, that marks the inefficient acceleration compared with losses. The cutoff in electron energy is therefore provided by the condition

$$t_{\rm acc}(\gamma) = t^T_{\rm IC}(\gamma) \rightarrow \bar\gamma^2 \simeq 2.0 \times 10^5 \times \left(\frac{6000\ K}{T_\star}\right)^4\left(\frac{C_r(R)}{200{\rm km\ s}^{-1}}\right)^2\frac{B(3\,R_\star)}{0.01G}\,\frac{r-1}{r^2 k_0}\,\frac{3R_\star}{R}, \quad (13)$$

or, equivalently, by $\bar{E} \simeq 0.2$ GeV at $R = 3R_\star$ and decreasing with R. Closer to the star, the radiative cooling timescale within the shock-heated plasma is shorter than the pulsation period. At larger distances from the star, the wind rarefaction leads to an increase of the radiative cooling timescale that becomes longer than the pulsation period. Such a transition can be used as a diagnostic to determine the distance from the star of X-ray enhancement region, as well as the local plasma density, and hence to constrain the stellar mass loss.

4.3. Nonthermal Component: Energy Range and Spectral Index

The spectral fit of the X-ray flux rapid enhancement in the range [0.4–8] keV performed herein shows a significant excess over the thermal emission and reveals the presence of a nonthermal power component along with the soft (thermal) X-ray.

The lower limit energy 0.8 keV used in the nonthermal spectral fit in Section 2 is based on the assumption that the nonthermal power law is produced by IC off the UV stellar photon radiation field (with a benchmark photon energy $\varepsilon_0 = 5$ eV). On the other end, the balance acceleration/energy losses for the electrons energized at the pulsation-driven shock sets a maximal electron energy as a function of the distance from the star ($\gamma \gtrsim 100$ from Equation (13)). The two conditions above read for the observed photon energy E (Rybicki & Lightman 1986)

$$4\,\gamma_1^2\,\varepsilon_0 \ll E \ll 4\,\gamma_2^2\,\varepsilon_0, \tag{14}$$

where the single-electron Lorentz factors γ_i, with $i = 1,2$, are the minimum and maximum values discussed above. Equation (14) leads to the constraints $80\,\mathrm{eV} \ll E \ll 200\,\mathrm{keV}$, hence the assumed lower limit $E = 0.8$ keV for the spectral fit. It is noteworthy that the electron spectrum is assumed not to change both γ_2 and spectral index while the shock swipes through the stellar wind close to the star, which applies as long as the energy losses do not dominate the shock acceleration.

Figure 5 shows that IC over the stellar UV ambient photon field dominates electron energy losses. The X-ray photon spectrum results from folding the electron differential energy spectrum $dN/d\gamma$ with the single-electron IC power in the Thomson regime (see Equation (6)). At low electron energies ($<10^5$ keV) and at timescales of tens of minutes (see Figure 5), the acceleration is faster than IC cooling; thus, the electron energy distribution is steadily replenished by freshly accelerated particles. At timescales of ∼hours, as the number of ∼GeV electrons increases, the IC cooling hampers further acceleration. Therefore, the electron energy spectrum cannot be assumed to be strictly in steady state at any time. However, because at timescales of a few days $t_{\rm acc} \sim t_{\rm IC}^T$, a near-balance between the two processes can be assumed.

The pulsating shock emission from the star is not expected to affect the spectral shape, due to the short cooling time by IC compared with the stellar pulsation time: electrons advected downstream of a shock lose most of their energy to the UV photons in the radiation field before encountering the subsequent shock (Chen & White 1991a). However, the energy spectrum of ions is not affected by energy losses, causing a buildup of high-energy ions population in the wind, due to crossing of multiple shocks traveling outward. Such an ion population might modify the turbulence in the wind at a variety of spatial scales and excite turbulence modes that increase the diffusion for ions accelerated by the subsequent shocks. Ions acceleration and turbulence excitation are not included herein.

4.4. IC Photon Energy Spectrum through the Stellar Corona

Over the narrow energy range (∼1 decade) considered herein, the differential electron spectrum $dN/d\gamma$ can be approximated by a power law, i.e., $dN/d\gamma = C\gamma^{-\delta}$ with a normalization constant C. A power-law component is also suggested by the observed energy spectral at photon energies $\gtrsim$1 keV (see Section 2). The observed photon spectrum is here calculated by folding $dN/d\gamma$ with the single-electron IC power off the photon blackbody distribution in the stellar wind $\mathrm{P}_{\rm IC}^T$ (Rybicki & Lightman 1986) defined in Equation (5).

The UV radiation field scattered photons and the energetic electrons are assumed to be isotropically distributed; if isotropy of electrons is not altered to the lowest order by the slow wind motion, the radially expanding wind UV field has to be isotropic (Chen & White 1991a). In the Thomson scattering limit ($\gamma\epsilon_0 \ll mc^2$), the IC scattered power per unit of volume and energy can be written as (Equation (7.31) Rybicki & Lightman 1986)

$$\frac{dE}{dVdt\;d\epsilon_1} = \frac{3\pi\sigma_T C}{h^3c^2}\bar{F}(\delta)(k_BT)^{(\delta+5)/2}E^{-\frac{\delta-1}{2}}, \tag{15}$$

where σ_T is the Thomson cross section, h the Planck constant, and $\bar{F}(\delta) \simeq 1$. Due to the scaling of the wind temperature $T(R) = T(R_\star)(R_\star/R)^{1/2}$, the photon flux per unit of energy emitted during the shock expansion between two radii R_i and R_f can be recast as

$$\begin{aligned} F(E;\,R_f,\,R_i) &= \frac{1}{E}\int_{R_i}^{R_f}\frac{dE}{dVdt\;d\epsilon_1}\left(\frac{R}{d}\right)^2 dR \\ &= \frac{3\pi\sigma_T C}{h^3c^2}\bar{F}(\delta)(k_BT)^{\frac{\delta+5}{2}}\frac{R_\star^3}{d^2}\frac{4}{7-\delta} \\ &\quad\times\left(\frac{R_f}{R_i}\right)^{(7-\delta)/4}E^{-\frac{\delta+1}{2}} \\ &\propto E^{-\frac{\delta+1}{2}}\quad[\frac{\mathrm{photons}}{\mathrm{cm^2\;s\;keV}}], \end{aligned} \tag{16}$$

where d is the Cepheid–Earth distance.

Thus, for an observed $F(E; R_f, R_i)$ flux per unit energy fitted by the nonthermal power law component with index Γ (see Section 2), the power-law index of the electrons energy distribution is $\delta = 2(\Gamma - 1) + 1$ (Rybicki & Lightman 1986). In Table 2, a thermal/nonthermal fit for the high state yields a reasonable $\chi^2 = 1.27$ by freezing $\Gamma \sim 2.0$, or a value of $\delta = 3.0$ that corresponds to a quite steep distribution of accelerated electrons. A value of $\Gamma \sim 1.6$, and hence $\delta = 2.2$, leads to a comparable $\chi^2 = 1.32$. The linear Diffusive Shock Acceleration model links the electron spectral index of the phase space distribution function s ($s = \delta + 2$) with the assumed energy-independent shock density compression $r = s/(s-3) \sim 2.5$ (and $r = 3.5$ for $\delta = 2.2$). For radiative shocks, the density compression depends on the particle energy because the thickness of the downstream cooling region is probed down to distinct distances from the shock at distinct particle energy (e.g., Krolik & Raymond 1985). This effect is neglected herein,

due to the near-balance of the cooling with the IC timescale shown in Figure 5.

4.5. Radio Synchrotron

The assumed magnetic field 0.01 G at a distance $3\,R_\star$ from the star implies a very long timescale for the radio synchrotron cooling that is therefore a very valuable constraint on the local magnetic field.

Radio continuum emission at 15 GHz (VLA) from δ Cep was reported by Matthews et al. (2020); the periodicity of such a radio emission is uncertain, hence its association with stellar pulsation. This radio data set seems to be consistent (Matthews & Evans 2023) with a time-variable radio emission at a level greater than or equal to 10%, but the likelihood of a correlation with the stellar pulsation seems to be very low.

5. Conclusions

We have presented an updated spectral fit of the thermal and nonthermal components of the enhanced X-ray emission observed by XMM-Newton in δ Cep (Engle et al. 2017). We propose a scenario of efficient local pre-ionization of the neutral stellar wind of δ Cep by a traveling pulsation-driven shock; shocks traveling through the same regions at a later time ($\sim t_p$) encounter a very hot and highly ionized plasma and efficiently accelerate electrons to multi-GeV. Our analysis of the acceleration and losses timescales, combined with previous hydrodynamic simulations (Moschou et al. 2020), suggests that IC over the UV background stellar field dominates the energy losses and limits the shock acceleration only as electrons reach the GeV energy range; the lack of periodic radio counterpart associated with stellar pulsation supports this scenario. The nonthermal emission powering the high-flux state does not seem to be completely shut off during the low-flux state. Although a two-temperature spectral fit is not statistically ruled out, we find that a significant nonthermal component is consistent with inferred parameters of star and circumstellar medium. If confirmed, this model lays the ground for the association of Cepheid pulsations with shock-accelerated GeV electrons.

Overall, multiwavelength (at least in X-rays, radio, and IR) coverage will help improve the understanding of the role of stellar pulsations in shaping the circumstellar material. If further X-ray observational campaigns for δ Cep, or other Cepheids, will identify a periodicity in X-ray flashes that are lagged by a fraction of the pulsation period from an FUV peak and originate in the near-star environment, additional constraints on the shock properties might be within reach. Furthermore, the exquisite spectral and imaging resolution of JWST from 0.7 to 10 μm might enable characterization with unprecedented precision of parameters such as size, distance from the star, gas density, and chemical composition of the interstellar clouds surrounding galactic Cepheids, leading the way to a better understanding of the particle acceleration in Cepheid environments.

We thank the referee for useful and constructive comments; we also thank Dr. S.P. Moschou for seminal work on this idea and for useful conversations. F.F. was supported, in part, by NASA through Chandra Theory Award Number TM0-21001X, TM6-17001A issued by the Chandra X-ray Observatory Center, which is operated by the Smithsonian Astrophysical Observatory for and on behalf of NASA under contract NAS8-03060, by NASA under grants 80NSSC18K1213 and by the NSF under grant 1850774. J.J.D. and N.R.E. were supported by NASA contract NAS8-03060 to the Chandra X-ray Center, and they thank the Director, Pat Slane, for continuing advice and support.

Appendix

The auxiliary functions for bremsstrahlung losses are defined as

$$A_p(E) = \gamma \ln\gamma + p - p/3 + p^3/\gamma^6(2/9\gamma^2 - 19/675\gamma p^2 - 0.06p^4/\gamma),$$
$$A_e(E) = p/\gamma(\gamma - 1)\Phi(E), \quad (17)$$

where $\Phi(E)$ is defined in Haug (2004),[6] Equation (7), as a piecewise function for distinct electron energy ranges.

ORCID iDs

Federico Fraschetti https://orcid.org/0000-0002-5456-4771
Konstantina Anastasopoulou https://orcid.org/0000-0002-3240-6609
Jeremy J. Drake https://orcid.org/0000-0002-0210-2276
Nancy Remage Evans https://orcid.org/0000-0002-4374-075X

References

Arnaud, K. A. 1996, in ASP Conf. Ser. 101, Astronomical Data Analysis Software and Systems V, ed. G. H. Jacoby & J. Barnes (San Francisco, CA: ASP), 17
Barron, J. A., Wade, G. A., Evans, N. R., Folsom, C. P., & Neilson, H. R. 2022, MNRAS, 512, 4021
Bohm-Vitense, E., & Love, S. G. 1994, ApJ, 420, 401
Chen, W., & White, R. L. 1991a, ApJ, 366, 512
Chen, W., & White, R. L. 1991b, ApJL, 381, L63
Cleeves, L. I., Bergin, E. A., Öberg, K. I., et al. 2017, ApJL, 843, L3
Colgan, J., Abdallah, J., Jr., Sherrill, M. E., et al. 2008, ApJ, 689, 585
Cuntz, M., & Luttermoser, D. G. 1990, ApJ, 353, L39
David, L., Fraschetti, F., Giacalone, J., et al. 2022, ApJ, 928, 66
Degenaar, N., Ballantyne, D. R., Belloni, T., et al. 2018, SSRv, 214, 15
Drake, J. J., Delgado, L., Laming, J. M., et al. 2016, ApJ, 825, 95
Drake, S. A., & Linsky, J. L. 1986, AJ, 91, 602
Drury, L. O. 1983, RPPh, 46, 973
Drury, L. O. 2011, MNRAS, 415, 1807
Engle, S. G., Guinan, E. F., Harper, G. M., et al. 2017, ApJ, 838, 67
Engle, S. G., Guinan, E. F., Harper, G. M., Neilson, H. R., & Evans, N. R. 2014, ApJ, 794, 80
Evans, N. R., Engle, S., Guinan, E., et al. 2018, in The RR Lyrae 2017 Conf. 6 Revival of the Classical Pulsators: from Galactic Structure to Stellar Interior Diagnostics, ed. R. Smolec, K. Kinemuchi, & R. I. Anderson (Warsaw: Polish Astronomical Society), 253
Evans, N. R., Pillitteri, I., Kervella, P., et al. 2021, AJ, 162, 92
Fraschetti, F. 2013, ApJ, 770, 84
Fraschetti, F. 2021, ApJ, 909, 42
Fraschetti, F., & Giacalone, J. 2012, ApJ, 755, 114
Fraschetti, F., & Giacalone, J. 2015, MNRAS, 448, 3555
Fraschetti, F., Katsuda, S., Sato, T., Jokipii, J. R., & Giacalone, J. 2018, PhRvL, 120, 251101
Fraschetti, F., & Pohl, M. 2017, EPJWC, 136, 02009
Gallenne, A., Mérand, A., Kervella, P., et al. 2021, A&A, 651, A113
Giacalone, J. 2005, ApJ, 624, 765
Giacalone, J., & Jokipii, J. R. 2007, ApJL, 663, L41
Gillet, D. 2014, A&A, 568, A72

[6] Figures 5 and 6 include our correction of a typo in Equation (7) therein, for the function $\Phi(E)$ in the range $E < 100$ keV.

Hampel, J., Komossa, S., Greiner, J., et al. 2022, RAA, 22, 055004
Haug, E. 2004, A&A, 423, 793
Hocdé, V., Nardetto, N., Lagadec, E., et al. 2020, A&A, 633, A47
Inoue, T., Yamazaki, R., Inutsuka, S.-i., & Fukui, Y. 2012, ApJ, 744, 71
Jokipii, J. R. 1982, ApJ, 255, 716
Jokipii, J. R. 1987, ApJ, 313, 842
Kervella, P., Mérand, A., Perrin, G., & Coude du Foresto, V. 2006, A&A, 448, 623
Krolik, J. H., & Raymond, J. C. 1985, ApJ, 298, 660
Kuntz, K. D., & Snowden, S. L. 2008, A&A, 478, 575
Landi, E., & Landini, M. 1999, A&A, 347, 401
Longair, M. S. 1994, High energy astrophysics Stars, Stars, the Galaxy and the interstellar medium the Galaxy and the interstellar medium, Vol. 2 (Cambridge: Cambridge Univ. Press)
Lucy, L. B. 1982a, ApJ, 255, 278
Lucy, L. B. 1982b, ApJ, 255, 286
Lucy, L. B., & Solomon, P. M. 1970, ApJ, 159, 879
Lucy, L. B., & White, R. L. 1980, ApJ, 241, 300
Markowitz, A. G., Nalewajko, K., Bhatta, G., et al. 2022, MNRAS, 513, 1662
Mathias, P., Gillet, D., Fokin, A. B., et al. 2006, A&A, 457, 575
Matthews, L. D., & Evans, N. R. 2023, arXiv:2301.04666
Matthews, L. D., Evans, N. R., & Rupen, M. P. 2020, AAS Meeting Abstracts, 235, 106.03
Matthews, L. D., Marengo, M., Evans, N. R., & Bono, G. 2012, ApJ, 744, 53
Meinecke, J., Doyle, H. W., Miniati, F., et al. 2014, NatPh, 10, 520
Mérand, A., Kervella, P., Coudé du Foresto, V., et al. 2006, A&A, 453, 155
Moschou, S. P., Vlahakis, N., Drake, J. J., et al. 2020, ApJ, 900, 157
Nardetto, N., Mourard, D., Kervella, P., et al. 2006, A&A, 453, 309
Owocki, S. P. 2015, AAS Meeting Abstracts, 412, 113
Parizot, E., Marcowith, A., Ballet, J., & Gallant, Y. A. 2006, A&A, 453, 387
Rybicki, G. B., & Lightman, A. P. 1986, Radiative Processes in Astrophysics (Weinheim,: Wiley-VCH)
Sasselov, D. D., & Lester, J. B. 1994, ApJ, 423, 795
Sato, T., Katsuda, S., Morii, M., et al. 2018, ApJ, 853, 46
Schlickeiser, R. 2009, MNRAS, 398, 1483
Scowcroft, V., Seibert, M., Freedman, W. L., et al. 2016, MNRAS, 459 1170
Uchiyama, Y., & Aharonian, F. A. 2008, ApJL, 677, L105
Wilkinson, T., & Uttley, P. 2009, MNRAS, 397, 666